

# Possible Chiral Topological Superconductivity in CrO<sub>2</sub> bilayers

Xu Dou, Kangjun Seo, and Bruno Uchoa\*

Department of Physics and Astronomy, University of Oklahoma, Norman, OK 73069, USA\*

(Dated: April 7, 2024)

We address the possible emergence of spin triplet superconductivity in CrO<sub>2</sub> bilayers, which are half-metals with fully spin-polarized conducting bands. Starting from a lattice model, we show that chiral  $p + ip$  states compete with non-chiral  $p$ -wave ones. At large doping, the  $p + ip$  channel has a sequence of topological phase transitions that can be tuned by gating effects and interaction strength. Among several phases, we find chiral topological phases having a single Majorana mode at the edge. We show that different topological superconducting phases could spontaneously emerge in the vicinity of the van-Hove singularities of the band.

**Introduction.** Half-metals such as CrO<sub>2</sub> [1, 2] are promising materials for the prospect of emergent topological superconductivity. By having a metallic Fermi surface with a single spin, they raise the possibility of chiral superconductivity in the triplet channel [3], which is believed to occur only in a handful of systems such as Sr<sub>2</sub>RuO<sub>4</sub> [4], which may have a spinfull triplet state, UPt<sub>3</sub> and some heavy fermions superconductors [5, 6]. A distinctive property of spin triplet chiral topological superconductivity is the presence of Majorana fermions propagating at the edges [7–12] and half-flux quantum vortices [15, 16] that can trap Majorana modes [13, 14]. Majorana edge states were predicted to exist in different heterostructures with strong spin-orbit coupling [17–22] and may have been recently observed in an anomalous Hall insulator-superconductor structure [23, 24].

In its most common form, CrO<sub>2</sub> is a three dimensional bulk material with rutile structure [25, 26]. It was recently suggested [28] that CrO<sub>2</sub>/TiO<sub>2</sub> heterostructures have fully spin polarized conduction bands over a wide energy window around the Fermi level, and behave effectively as a two dimensional (2D) crystal. In its simplest 2D form, CrO<sub>2</sub> will form a bilayer. It is natural to ask if this material could spontaneously develop 2D chiral topological superconducting phases and host Majorana fermions [17].

We start from a lattice model for a single CrO<sub>2</sub> bilayer to address the formation of spin triplet pairs either with  $p$ -wave or  $p_x + ip_y$  symmetry, which leads to a fully gapped state. Due to the strong anisotropy of the gap, the superconducting order has a line of quantum critical points as a function of both doping and coupling strength. In the  $p + ip$  state, we show that the system has an exotic sequence of topological phase transitions, that could be tuned with gating effects. Different non-trivial topological phases may occur in the vicinity of van-Hove singularities of the band, where the density of states (DOS) diverges, allowing the possibility for both conventional and purely electronic mechanisms. We suggest that this system may provide an experimental realization of intrinsic 2D chiral topological superconductivity in the triplet channel.

**Lattice model.** In a bilayer system, the Cr atoms form

two interpenetrating square sublattices,  $A$  and  $B$ , each one sitting on a different layer. From above, the Cr atoms are arranged in a checkerboard pattern, as shown in Fig. 1. Each site on sublattice  $A$  ( $B$ ) has two orbitals with  $d_{xy}$  and  $d_{xz}$  ( $d_{yz}$ ) symmetry. Nearest neighbors (NN) hopping between a  $d_{xy}$  orbital in sublattice  $B$  with a  $d_{xz}$  orbital in sublattice  $A$  has amplitude  $t_1$  along the the  $(1, \bar{1})$  direction and zero along the  $(1, 1)$  direction by symmetry. In the same way, NN hopping between a  $d_{xy}$  orbital in sublattice  $A$  and with a  $d_{yz}$  orbital in  $B$  has

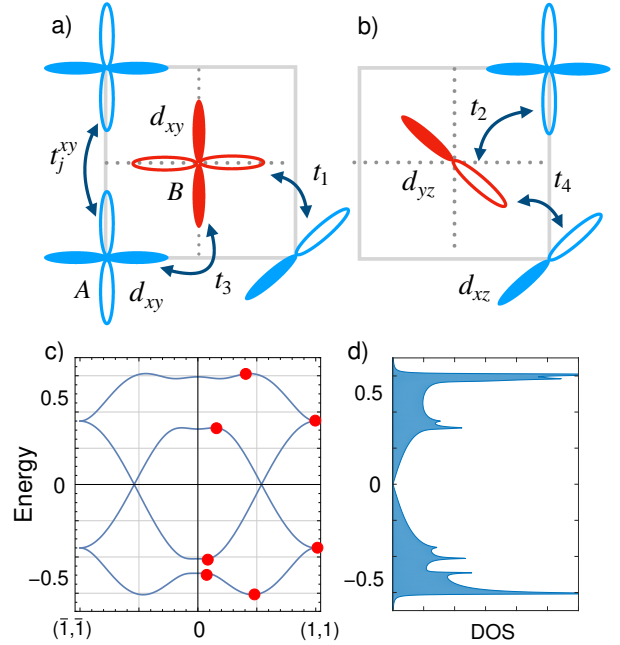


Figure 1. (Color online) top: Lattice of a CrO<sub>2</sub> bilayer, with  $d_{xy}$  and  $d_{xz}$  ( $d_{yz}$ ) orbitals in sublattice  $A$  ( $B$ ). The blue orbitals sit in the top layer ( $A$  sites), and red orbitals in the lower one ( $B$  sites). Hopping energies are indicated by  $t_j^\alpha$  for intra-orbital hopping between next-nearest sites, with  $\alpha = xy, xz$  for  $j = A$  and  $\alpha = xy, yz$  for  $j = B$ , and  $t_i$  ( $i = 1, 2, 3, 4$ ) for nearest neighbor hopping. c) Energy spectrum of the lattice model along the diagonal  $(1, 1)$  direction. Energy axes in eV units. Red dots indicate the location of van Hove singularities, where the DOS (d) diverges logarithmically.

amplitude  $t_2$  along the  $(1, 1)$  direction and zero along the other diagonal in the  $xy$  plane. Intra-orbital NN hopping is finite between  $d_{xy}$  orbitals ( $t_3$ ) but zero between  $d_{xz}$  and  $d_{yz}$  orbitals ( $t_4$ ), which are orthogonal to each other. Among next-nearest neighbors (NNN), the dominant processes are described by intra-orbital hoppings  $t_j^\alpha$ , with  $\alpha = xy, xz$  for sites in sublattice  $j = A$  and  $\alpha = xy, yz$  for  $B$  sites.

The Hamiltonian can be described in a four component basis  $\Psi = (\psi_{A,xy}, \psi_{A,xz}, \psi_{B,xy}, \psi_{B,yz})$ . In momentum space,  $\mathcal{H}_0 = \sum_{\mathbf{q}} \Psi_{\mathbf{q}}^\dagger h(\mathbf{q}) \Psi_{\mathbf{q}}$ , with [28]

$$h(\mathbf{q}) = \begin{pmatrix} h_A & h_{AB} \\ h_{AB}^\dagger & h_B \end{pmatrix}, \quad (1)$$

where

$$h_A = \begin{pmatrix} \epsilon_A^{xy}(\mathbf{q}) & 0 \\ 0 & \epsilon_A^{xz}(\mathbf{q}) \end{pmatrix}, h_B = \begin{pmatrix} \epsilon_B^{xy}(\mathbf{q}) & 0 \\ 0 & \epsilon_B^{yz}(\mathbf{q}) \end{pmatrix}. \quad (2)$$

The diagonal terms incorporate NNN hopping processes, where  $\epsilon_j^\alpha(\mathbf{q}) = E_j^\alpha + 4t_j^\alpha \cos q_x \cos q_y$ , with  $E_j^\alpha$  a local potential on orbital  $\alpha$  in sublattice  $j$  and  $q_{x,y} = \frac{1}{2}(k_x \mp k_y)$  the momentum along the two diagonal directions of the crystal. The off-diagonal terms in (1) describe the NN hopping terms illustrated in panels a) and b) in Fig. 1,

$$h_{AB} = \begin{pmatrix} -2t_3 \sum_{\nu=x,y} \cos q_\nu & 2it_1 \sin q_y \\ 2it_2 \sin q_x & -2t_4 \sum_{\nu=x,y} \cos q_\nu \end{pmatrix}, \quad (3)$$

where  $t_4 = 0$  in the absence of spin-orbit coupling.

The energy spectrum is shown in Fig. 1c, and has two sets of Dirac points along the  $(1, 1)$  and  $(1, \bar{1})$  directions, respectively. Enforcing the symmetries of the 2D lattice, namely roto-inversion  $S_4$  symmetry and mirror symmetry  $M$  at the diagonal directions of the unit cell, we adopt  $t_1 = -t_2 \equiv t \sim 0.3\text{eV}$  as the leading energy scale, and the set of parameters  $t_3 \sim t/30$ ,  $t_j^{xy} = -t_A^{xz} = -t_B^{yz} \sim t/3$ , and  $E_j^{xy} = -E_A^{xz} = -E_B^{yz} \sim t/6$ . We also use  $t_4 \sim it/8$ , following ab initio results [27, 28]. The four band model breaks down near the edge of the band, where states may hybridize with high energy bands. We also assume that the bands are spinless. The resulting band structure has several van Hove singularities at the saddle points, where the density of states (DOS) diverges logarithmically, as depicted in Fig. 1d. In the vicinity of those points (red dots), the system can be unstable towards superconductivity.

*Pairing Hamiltonian.* For spinless fermions, superconductivity is allowed only in the triplet channel. The wavefunction of the Cooper pairs is anti-symmetric under inversion, and hence only states with odd angular momentum are allowed. When electrons pair across the center of the Brillouin zone, the lowest symmetry is in the  $p$ -wave channel, which can be induced by NN pairing.  $f$ -wave pairing may be induced with NNN pairing only. This channel is subdominant and will not be addressed.

We consider the possible instabilities of the lattice model both in the  $p$ -wave and in the chiral  $p + ip$  state, which can produce a full gap. A conclusive assessment of the stability of those states requires taking fluctuations into account [29–31], which will be considered elsewhere.

For NN sites, the effective interaction term has the form

$$\mathcal{H}_{\text{int}} = -\frac{1}{2} \sum_{\mathbf{r} \in \text{NN}} g^{\alpha\beta} \hat{n}_{i,\alpha}(\mathbf{r}_i) \hat{n}_{j,\beta}(\mathbf{r}_j) \quad (4)$$

where  $\hat{n}_{i,\alpha} = \psi_{i,\alpha}^\dagger \psi_{i,\alpha}$  is the density operator in orbital  $\alpha$  on sublattice  $i = A, B$ ,  $g^{\alpha\alpha} \equiv g_1 > 0$  is the intra-orbital coupling, and  $g^{xy,yz} = g^{xz,xy} \equiv g_2 > 0$  is the coupling in the inter-orbital channel. The  $p + ip$  pairing follows from the Ansatz on the lattice  $\Delta^{\alpha\beta}(\delta_n) = g^{\alpha\beta} \langle \psi_{A,\alpha}(\mathbf{r}) \psi_{B,\beta}(\mathbf{r} + \vec{\delta}_n) \rangle \equiv \Delta^{\alpha\beta} e^{i\frac{\pi}{2}n}$ , where  $\vec{\delta}_{1,3} = \pm \frac{a}{2}(\hat{x} + \hat{y})$  and  $\vec{\delta}_{2,4} = \pm \frac{a}{2}(\hat{x} - \hat{y})$  describe the four NN vectors, with  $a$  the lattice constant. For  $p$ -wave pairing, we use the Ansatz  $\Delta^{\alpha\beta}(\pm \delta_{1,2}) \equiv \pm \Delta^{\alpha\beta}$ .

Defining  $\Delta^{\alpha\alpha} \equiv \Delta_1$  and  $\Delta^{\alpha\beta} \equiv \Delta_2$  for intra-orbital and inter-orbital pairing respectively, the order parameter in momentum space  $\Delta_i^C(\mathbf{q}) = \Delta_i^C(\sin q_y + i \sin q_x)$  has chiral  $p_x + ip_y$  symmetry, with  $i = 1, 2$  and  $q_{x,y}$  defined as above Eq. (3). In the non-chiral state,  $\Delta_i^p(\mathbf{q}) = \Delta_i^p(\sin q_y + \sin q_x)$  has  $p_x$  symmetry [32]. At the mean field level, Hamiltonian (1) and (4) result in the Bogoliubov-de Gennes (BdG) Hamiltonian  $\mathcal{H}_{\text{BdG}} = \sum_{\mathbf{k} \in \text{BZ}} \Phi_{\mathbf{k}}^\dagger h_{\text{BdG}}(\mathbf{q}) \Phi_{\mathbf{k}}$  with  $\Phi_{\mathbf{k}} = (\Psi_{\mathbf{k}}, \Psi_{-\mathbf{k}}^\dagger)$ , which has the form

$$h_{\text{BdG}}(\mathbf{q}) = \begin{pmatrix} h(\mathbf{q}) & \hat{\Delta}(\mathbf{q}) \\ \hat{\Delta}^\dagger(\mathbf{q}) & -h^T(-\mathbf{q}) \end{pmatrix}, \quad (5)$$

where

$$\hat{\Delta}(\mathbf{q}) = \begin{pmatrix} 0 & \Delta_1(\mathbf{q})\mathbf{1} + \Delta_2(\mathbf{q})\sigma_x \\ \Delta_1(\mathbf{q})\mathbf{1} + \Delta_2(\mathbf{q})\sigma_x & 0 \end{pmatrix} \quad (6)$$

is the pairing matrix, with  $\sigma_x$  a Pauli matrix in the orbital space. Minimization of the free energy  $\mathcal{F}(\Delta_1, \Delta_2) = -T \text{tr} \sum_{\mathbf{k}} \ln e^{-h_{\text{BdG}}(\mathbf{k})/T} + \sum_{i=1,2} |\Delta_i|^2/g_i$  for a fixed chemical potential  $\mu$  gives the zero temperature ( $T = 0$ ) phase diagram shown in Fig. 2a, b as a function of the couplings  $g_1$  and  $g_2$ . The two leading instabilities in the  $p$ -wave and chiral  $p + ip$  states compete with each other and are addressed below.

*p-wave phase.* The vertical line in fig. 2a describes a quantum phase transition at  $g_1 = \tilde{g}_{1c}(\mu)$  separating the normal phase (N) from the intra-orbital  $p_x$  state ( $p\text{SC I}$ ). At  $g_2 = \tilde{g}_{2,c}(\mu)$  (dashed line) the system has a first order phase transition towards an inter-orbital  $p$ -wave state ( $p\text{SC II}$ ). The due to the anisotropy of the  $p$ -wave gap, the curve  $g = \tilde{g}_{1c}(\mu)$  depicted in Fig. 3a describes a line quantum critical points with power law scaling [33]. The intra-orbital channel ( $\Delta_1^p \neq 0$ ) dominates over the inter-orbital one for all values of  $\mu$ . At the mean field level, it is

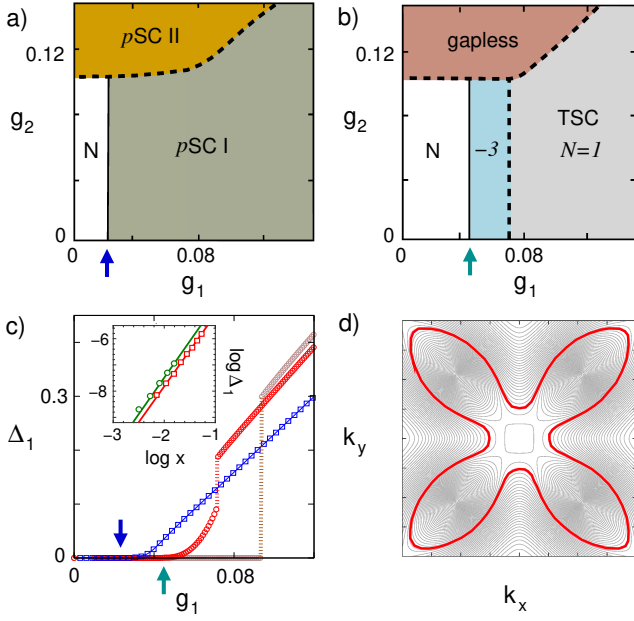


Figure 2. (Color online) Phase diagram for a)  $p$ -wave and b)  $p + ip$  state for intra-orbital ( $g_1$ ) and inter-orbital ( $g_2$ ) couplings at  $\mu = 4t/3 = 0.4$  eV.  $g_1$  and  $g_2$  in eV units. Green area: intra-orbital  $p$ -wave (pSC I) for  $g > \tilde{g}_{1c}(\mu)$ . Yellow: inter-orbital  $p$ -wave (pSC II). Gray area: strong coupling topological phase (TSC) with Chern number  $\mathcal{N} = 1$ ; Light blue: gapped weak coupling one ( $\tilde{g}_{1c} < g < g_{1c}$ ) with  $\mathcal{N} = -3$  (see Fig. 3b). Light red: gapless  $p + ip$ , which is topologically trivial. Dashed lines: first order phase transitions. Solid black lines: second order transition (blue and green arrows). c) Scaling of  $\Delta_1$  vs  $g_1$ . Red and brown circles:  $p + ip$  for  $\mu = 0.4$ , and 0, respectively. Blue square:  $p$ -wave for  $\mu = 0.4$  eV. Green and blue arrows: critical coupling  $\tilde{g}_{1c} \approx t/7 = 0.045$  eV and  $\tilde{g}_{1c} \approx t/12 = 0.025$  eV respectively for  $\mu = 0.4$  eV. Inset:  $\Delta_1^C$  vs  $\log x$ , with  $x = (1 - \tilde{g}_{1c}/g)$ , showing power law scaling in the chiral phase near  $\tilde{g}_{1c}(\mu)$ . Green dots:  $\mu = 0.3$  eV. Red:  $\mu = 0.4$  eV. d) Brillouin zone. Red line: anisotropic Fermi surface at  $\mu = 0.33$  eV.

also the leading instability in the weak coupling regime of the problem (which we define below), and subleading to the  $p + ip$  state in the strong coupling sector, as indicated in Fig. 3a.

**$p + ip$  phase.** The inter-orbital channel  $g_2$  may lead to gapless chiral  $p + ip$  superconductivity ( $\Delta_2^C \neq 0$ ) shown in the red region, which is topologically trivial (Fig. 2a). This state dominates over the inter-orbital pSC II phase, shown in Fig. 2b. The dashed line around the gapless phase in Fig. 2b describes a first order phase transition and sets the boundary of the gapless  $p + ip$  phase with the others at  $g_2 = g_{2c}(\mu)$ . The intra-orbital  $p + ip$  pairing state ( $\Delta_1^C \neq 0$ ) on the other hand is fully gapped and can be topological.

The gapped state has multiple minima that compete. The dashed vertical line in Fig. 2b indicates a first order phase transition between the weak and strong coupling topological phases (TSC) at  $g_1 = g_{1c}(\mu)$ . At this cou-

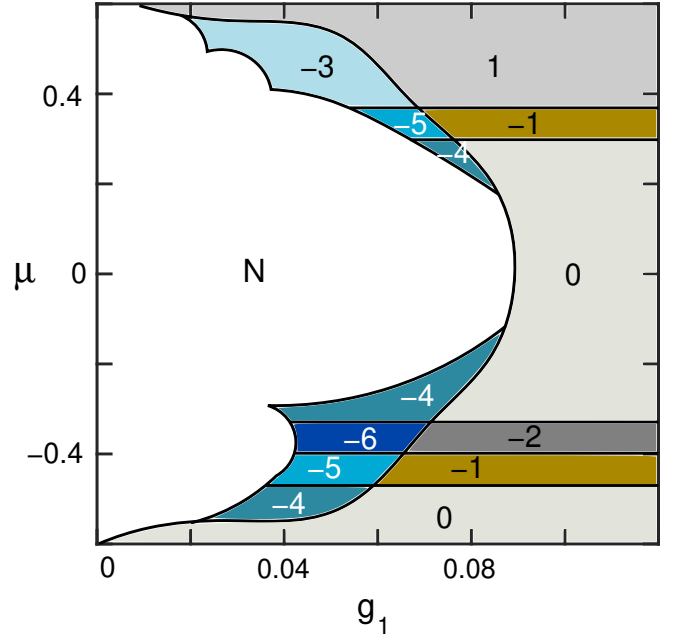


Figure 3. (Color online) Mean field phase diagram as a function of the chemical potential  $\mu$  and intra-orbital pairing coupling  $g_1$ , both in eV units. The phase diagram does not depend on  $g_2$  for  $g_2 \lesssim 0.1$  eV (see Fig 2). a) Normal phase (N),  $p_x$  superconducting phase (pSC I), chiral  $p + ip$  state (CSC) and topological  $p + ip$  phase (TSC). b) Possible topological phases in the chiral  $p + ip$  channel. The integers indicate the corresponding BdG Chern number  $\mathcal{N}$ . For fixed  $g_1$ , the system has a sequence of topological phase transitions near the van-Hove singularities of the band, where the topology of the Fermi surface changes. The blue regions correspond to the weak coupling gapped  $p + ip$  phases, which are topological. Gray and maroon regions: strong coupling phases. In mean field, the gapped  $p + ip$  state wins over the non-chiral  $p$  state in the strong coupling sector.

pling, the superconducting order parameter  $\Delta_1^C$  jumps (see Fig. 2c) and different gapped phases with distinct topological numbers coexist. The resulting gap is very anisotropic around the Fermi surface (Fig. 2d). In the weak coupling phase  $\tilde{g}_{1c}(\mu) < g < g_{1c}(\mu)$  shown in the light blue region in Fig. 2b, the intra-orbital chiral gap  $\Delta_1^C$  scales as a power law with the coupling for fixed  $\mu$ ,

$$\Delta_1^C(g_1) \propto (1 - \tilde{g}_{1c}/g)^\beta, \quad (7)$$

with  $\beta \approx 2.7 \pm 0.1$  for  $0.2 \lesssim \mu \lesssim 0.4$  eV (see Fig. 2c inset).  $\Delta_1^C$  vanishes at the critical coupling  $\tilde{g}_{1c}$ , where the system has a second order phase transition to the normal state, indicated by the green arrows in Fig. 2. A qualitatively similar behavior is also observed in the scaling of the intra-orbital  $p$ -wave gap  $\Delta_1^P$  near the critical coupling  $\tilde{g}_1(\mu)$  (blue arrows in Fig 2) [33].

When  $\mu$  is in the immediate vicinity of the van Hove singularities,  $\tilde{g}_{1c}$  abruptly drops towards zero. This singular behavior suggests a crossover to exponential scaling

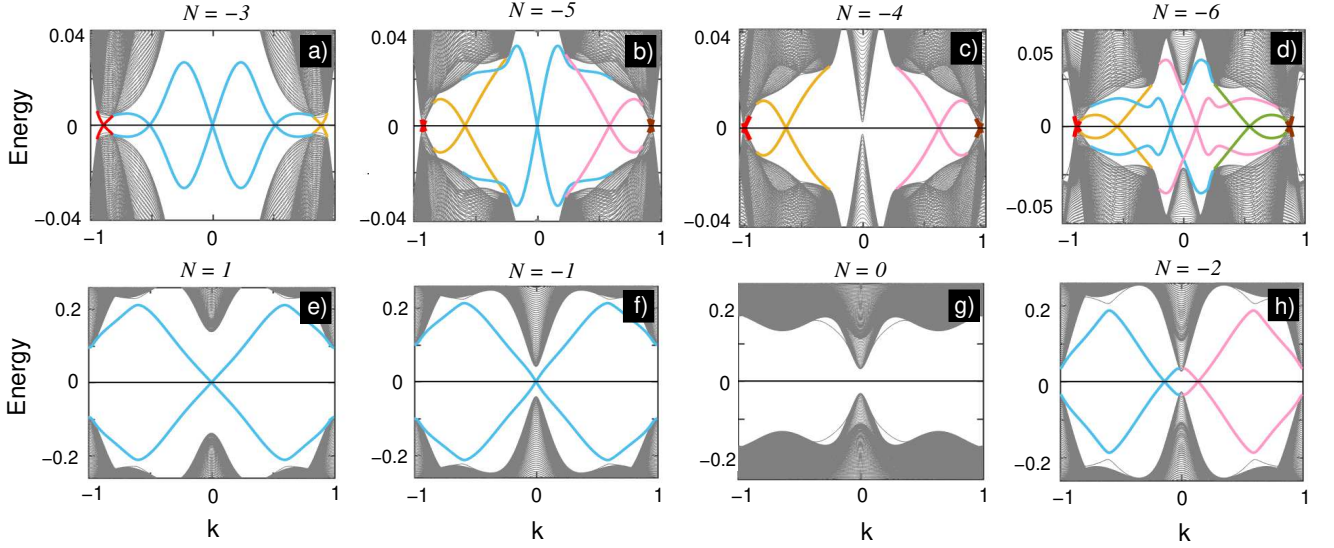


Figure 4. (Color online) Majorana edge modes in the different topological phases in the gapped  $p+ip$  state. Energy units in eV. a) BdG Chern number  $\mathcal{N} = -3$  state, at  $\mu = 0.44\text{eV}$ . b)  $\mathcal{N} = -5$  at  $\mu = 0.33\text{eV}$ ; c)  $\mathcal{N} = -4$  at  $\mu = -0.49\text{ eV}$  and d)  $\mathcal{N} = -6$  at  $\mu = -0.38\text{ eV}$  in the weak coupling regime. The lower panels give the corresponding phases in the strong coupling sector: e)  $\mathcal{N} = 1$  at  $\mu = 0.44\text{eV}$ , f)  $\mathcal{N} = -1$  at  $\mu = 0.33\text{eV}$ ; g)  $\mathcal{N} = 0$  at  $\mu = -0.49\text{ eV}$ , which is topologically trivial and h)  $\mathcal{N} = -2$  at  $\mu = -0.38\text{eV}$ . At the crossing from the weak to strong coupling phases, when  $g = g_{1c}(\mu)$ , all Chern numbers increase by 4.

when the Fermi surface is nested at the van Hove singularities [33]. In that regime, the phase transition is not quantum critical. A similar behavior is also observed in the  $p\text{SC}$  I phase near the van Hove. At the saddle points, the order parameter can be broken into four patches related by the  $C_4$  symmetry of the bands combined with odd angular momentum of the Cooper pairs. By symmetry, the free energy written in a basis of  $p_x$  and  $p_y$  pairing states is

$$\mathcal{F}(\Delta_x^p, \Delta_y^p) = \alpha(|\Delta_x^p|^2 + |\Delta_y^p|^2) + \beta(|\Delta_x^p|^2 + |\Delta_y^p|^2)^2 - \frac{\beta}{2}|(\Delta_x^p)^2 - (\Delta_y^p)^2|^2 + \mathcal{O}(\Delta^6), \quad (8)$$

where  $\alpha < 0$  in the ordered state and  $\beta > 0$  [34]. The last term favors coexistence between  $\Delta_x^p$  and  $\Delta_y^p$  with  $\pm\pi/2$  phase difference ( $p+ip$  phase), while the second one favors a non-chiral  $p$  state. The chiral and non-chiral phases are exactly degenerate at the mean field level up to quartic order terms in the expansion. Their degeneracy will likely be lifted by fluctuations, which will be addressed elsewhere.

In general, all the gapped chiral phases prevail over the gapless one ( $\Delta_2^C$ ). At small doping, the two critical couplings of the weak and strong coupling phases merge ( $\bar{g}_{1c} = g_{1c}$ ) below  $|\mu| \lesssim 0.6t$  and the gapped phase has a first order phase transition to the normal state at  $g < g_{1c}(\mu)$  (see Fig 3b).

*Topological phase transitions.* In 2D, spinless superconductors with a bulk gap that breaks time reversal symmetry belong to the C class in the ten-fold classification table [36, 37]. The topological number in this

class is defined by the BdG Chern number  $\mathcal{N}$ , which corresponds to the number of chiral Majorana modes propagating along the edge [7, 38].

In Fig. 3b, we explicitly calculate the Chern number

$$\mathcal{N} = (i/2\pi) \int_{BZ} d^2\mathbf{q} \Omega_z(\mathbf{q}) \quad (9)$$

in the gapped state as a function of  $\mu$  and intra-orbital coupling  $g_1$ , with  $\Omega(\mathbf{q}) = \nabla_{\mathbf{q}} \times \langle \psi_{n,\mathbf{q}} | \nabla_{\mathbf{q}} | \psi_{n,\mathbf{q}} \rangle$  the Berry curvature from the eigenstates of the BdG Hamiltonian at the Fermi level,  $|\psi_{n,\mathbf{q}}\rangle$ . By changing the chemical potential, the system shows a sequence of topological phase transitions.

In the weak coupling phase, shown in the blue areas in Fig. 3b, there are up to five transitions separating different topological phases with  $\mathcal{N} = -4, -5, -6, -4, -5$ , and  $-3$ , in the range of  $-2t \leq \mu \leq 2t = 0.6\text{eV}$ . The critical values of the chemical potential where the system has a topological phase transition are close to the energy of the van Hove singularities of the band (see Fig. 1c) and coincide with the energies where the topology of the Fermi surface changes. At those critical values, the superconducting gap closes and the Chern number jumps by an integer number. The line  $g_1 = \bar{g}_{1c}(\mu)$  separates the blue areas from the normal region through continuous phase transitions. As anticipated, when  $|\mu| \lesssim 0.6t = 0.18\text{eV}$ ,  $\bar{g}_{1c} = g_{1c}$ , and the weak coupling phases are suppressed. The singular behavior of  $\bar{g}_{1c}(\mu)$  when  $\mu$  is at the van Hove is not captured by the numerics shown in Fig. 3 due to the smallness of the gap.

The solid curve separating the blue regions in Fig. 3b from the strong coupling phases sets  $g_{1c}(\mu)$ , which de-



scribes a line of first order phase transitions between different gapped phases. At this line, the order parameter is discontinuous [35], indicating the onset of a topological phase transition as a function of  $g_1$  for fixed  $\mu$ . In all cases, the Chern number changes across the  $g_{1c}(\mu)$  line by  $\Delta\mathcal{N} = 4$ . Deep in the strong coupling regime (gray and maroon regions), for fixed  $g > g_{1c}(\mu = 0)$ , there are six topological phase transitions separating the phases  $\mathcal{N} = 0, -1, -2, 0, -1, 1, 0$  as a function of the chemical potential. The  $\mathcal{N} = 0$  phases (CSC) are chiral but topologically trivial. At the wide doping window  $1.27t \lesssim \mu \lesssim 2t = 0.6$  eV, the elemental chiral topological superconducting phase with  $\mathcal{N} = \pm 1$ , and hence a single Majorana mode, can emerge at strong coupling.

*Chiral Majorana edge states.* To explicitly verify the Chern numbers for the different phases, we calculate the edge modes of the gapped state in a two dimensional strip geometry with edges oriented along the  $(1, 0)$  direction.

The plots in Fig. 4a–d (top row) show the evolution of the edge modes in the weak coupling regime ( $\bar{g}_{1c} < g < g_c(\mu)$ ) for different values of  $\mu$ . The  $\mathcal{N} = -3$  state shown in Fig. 4a has five edge modes in total, but only three modes that are topologically protected, as indicated by the three different colors. The three modes indicated in blue can be adiabatically deformed into a single zero energy crossing at  $k = 0$ , and hence count as a single topologically protected mode. By decreasing the chemical potential into the contiguous  $\mathcal{N} = -5$  state (Fig. 4b), two of those modes become topologically protected, raising the number of Majorana modes to five. By reducing  $\mu$  further into the  $\mathcal{N} = -4$  state, the topology of the Fermi surface changes drastically, forming gapped pockets of charge around four Dirac nodes, indicated in Fig. 1c. Panel d shows the edge modes of the  $\mathcal{N} = -6$  state, for  $\mu \lesssim -t = -0.3$  eV. The corresponding edge modes in the strong coupling regime ( $g > g_{1c}(\mu)$ ) with  $\mathcal{N} = 1, -1, 0$ , and  $-2$  are shown in the bottom row of Fig. 4 (e–h).

*Pairing Mechanism.* Although it is difficult to reliably predict a mechanism of superconductivity, at large doping and in the vicinity of the van Hove singularities, where the DOS is very large, both phonons and electronic interactions could be suitable candidates for a pairing mechanism. We will not discuss the phonon mechanism, since it is conventional.

Electronic mechanisms typically provide attraction when the charge susceptibility at the Fermi surface nesting vector  $\mathbf{Q}$  satisfies  $\chi(\mathbf{Q}) > \chi(0)$  [39]. When the chemical potential  $\mu$  is close to a Van Hove singularity, the electronic bands have energy spectrum  $\epsilon(\mathbf{q}) = -\alpha q_x^2 + \beta q_y^2$ , ( $0 < \alpha \leq \beta$ ) where  $\mathbf{q}$  is the momentum away from the saddle point. The susceptibility in the vicinity of the singularity is logarithmic divergent,  $\chi(0) = \frac{1}{2\pi^2} \sqrt{\alpha\beta} \ln(\Lambda/\delta\mu)$  with  $\delta\mu$  the deviation away from the van Hove and  $\Lambda \sim t$  an ultraviolet cut-off around the saddle point [40]. At the nesting wavevec-

tor  $\epsilon(\mathbf{q} + \mathbf{Q}) = -\alpha p_y^2 + \beta p_x^2$ , the susceptibility is

$$\chi(\mathbf{Q}) = c/(\alpha + \beta) \ln(\Lambda/\delta\mu), \quad (10)$$

where the constant  $c = \frac{1}{\pi^2} \ln(\sqrt{\frac{\alpha}{\beta-\alpha}} + \sqrt{\frac{\beta}{\beta-\alpha}})$  is logarithmically divergent at the nesting condition  $\alpha = \beta$  [41]. For the particular lattice Hamiltonian parametrization taken from Ref. [28], the fitting of the bands around the van Hove at  $\mu = 0.312$  eV has  $\alpha \approx 1.2$  and  $\beta \approx 1.7$ . That gives the ratio  $\chi(\mathbf{Q})/\chi(0) \sim 1.20$ , suggesting that a purely electronic mechanism of superconductivity is possible [40, 42, 43]. The high doping regime could in principle be reached with gating effects for  $\text{CrO}_2$  encapsulated in an insulating substrate [44] that preserves the roto-inversion symmetry of the lattice.

*Acknowledgements.* BU acknowledges K. Mullen for discussions. XD, KS and BU acknowledge NSF CAREER Grant No. DMR-1352604 for partial support.

---

\* uchoa@ou.edu

- [1] Yu. S. Dedkov, M. Fonine, C. König, U. Rüdiger, and G. Güntherodt, Appl. Phys. Lett. **80**, 4181 (2002).
- [2] R. J. Soulen, J. M. Byers, M. S. Osofsky, B. Nadgorny, T. Ambrose, S. F. Cheng, P. R. Broussard, C. T. Tanaka, J. Nowak, J. S. Moodera, A. Barry, and J. M. D. Coey, Science **282**, 85 (1998).
- [3] W. E. Pickett, Phys. Rev. Lett. **77**, 3185 (1996).
- [4] A. P. Mackenzie and Y. Maeno, Rev. Mod. Phys. **75**, 657 (2003).
- [5] C. Kallin and J. Berlinsky, Rep. Prog. Phys. **79**, 54502 (2016).
- [6] Y. Maeno, S. Kittaka, T. Nomura, S. Yonezawa, K. Ishida, J. Phys. Soc. Jpn. **81**, 011009 (2012).
- [7] N. Read and D. Green Phys. Rev. B **61**, 10267 (2000).
- [8] X.-L. Qi, T. L. Hughes, S. Raghu, and S.-C. Zhang, Phys. Rev. Lett. **102**, 187001 (2009).
- [9] X.-L. Qi, and S.-C. Zhang, Rev. Mod. Phys. **83**, 1057 (2011).
- [10] J. Alicea, Rep. Prog. Phys. **75**, 076501 (2012).
- [11] P. A. Lee, Science **346**, 545-546 (2014).
- [12] M. Sato and Y. Ando, Rep. Prog. Phys. **80**, 076501 (2017).
- [13] R. Jackiw and P. Rossi, Nucl. Phys. B **190**, 681 (1981).
- [14] J. P. Xu *et al.*, Phys. Rev. Lett. **114**, 017001 (2015).
- [15] S. B. Chung, H. Bluhm, and E.-A. Kim, Phys. Rev. Lett. **99**, 197002 (2007).
- [16] J. Jang, D. G. Ferguson, V. Vakaryuk, R. Budakian, S. B. Chung, P. M. Goldbart, Y. Maeno, Science **331**, 186 (2011).
- [17] L. Fu and C. L. Kane Phys. Rev. Lett. **100**, 096407 (2008).
- [18] A. R. Akhmerov, Johan Nilsson, and C. W. J. Beenakker, Phys. Rev. Lett. **102**, 216404 (2009).
- [19] L. Fu, C. L. Kane, Phys. Rev. Lett. **102**, 216403 (2009).
- [20] R. M. Lutchyn, J. D. Sau, and S. Das Sarma, Phys. Rev. Lett. **105**, 077001 (2010).
- [21] S. B. Chung, H.-J. Zhang, X.-L. Qi, and S.-C. Zhang, Phys. Rev. B **84**, 060510(R) (2011).

- [22] J. Li, T. Neupert, Z. J. Wang, A. H. MacDonald, A. Yazdani, B. A. Bernevig, Nat. Comm. **7**, 12297 (2016).
- [23] X.-L. Qi, T. L. Hughes, and S.-C. Zhang, Phys. Rev. B **82**, 184516 (2010).
- [24] Q. L. He *et al.*, Science **357**, 294 (2017).
- [25] K. Schwarz, Journal of Physics F-Metal Physics **16**, L211 (1986).
- [26] M.I. Katsnelson, V.Yu. Irkhin, L. Chioncel, A.I. Lichtenstein, R.A. de Groot, Rev. Mod. Phys. **80**, 315 (2008).
- [27] While  $t_4 = 0$  by the symmetry of the crystal, spin-orbit coupling effects lead to a finite imaginary  $t_4 = it/8 \approx \pm(i)0.036$  eV. See Ref. [28]. This term opens a small gap of  $\sim 4$  meV at the Dirac nodes.
- [28] T. Cai, X. Li, F. Wang, S. Ju, J. Feng, and C.-D. Gong, Nano Lett. **15**, 6434 (2015).
- [29] N. Furukawa, T. M. Rice, and M. Salmhofer, Phys. Rev. Lett. **81**, 3195 (1998).
- [30] R. Nandkishore, L. S. Levitov and A. V. Chubukov, Nat. Phys. **8**, 158 (2012).
- [31] M. L. Kiesel, C. Platt, W. Hanke, D. A. Abanin, and R. Thomale, Phys. Rev. B **86**, 020507(R) (2012).
- [32] The  $p_y$  state is also allowed by symmetry. All non-chiral combinations of  $p_x$  and  $p_y$  pairing symmetry have higher energy and are subdominant.
- [33] For a more detailed analysis of the quantum critical scaling, see supplementary materials.
- [34] For a symmetry analysis, see supplementary materials.
- [35] The spectral gap does not close along the line of first order topological phase transitions. The gap closes, however, if  $\Delta_1$  is virtually changed as a continuous parameter connecting two topologically distinct ground states.
- [36] A. P. Schnyder, S. Ryu, A. Furusaki, and A. W. W. Ludwig, Phys. Rev. B **78**, (2008).
- [37] S. Ryu, A. Schnyder, A. Furusaki, and A. Ludwig, New J. Phys. **12**, 65010 (2010).
- [38] D. J. Thouless, M. Kohmoto, M. P. Nightingale, M. de Nijs, Phys. Rev. Lett. **49**, 405 (1982).
- [39] W. Kohn, J. M. Luttinger, Phys. Rev. Lett. **15**, 524 (1965).
- [40] J. Gonzalez, Phys. Rev. B **78**, 205431 (2008).
- [41] P. C. Pattnaik, C. L. Kane, D. M. Newns, C. C. Tsuei, Phys. Rev. B **45**, 5714 (1992).
- [42] F. Guinea, B. Uchoa, Phys. Rev. B **86**, 134521 (2012).
- [43] This mechanism does not in principle discard the possibility of particle-hole instabilities. In the square lattice, they are known to be subleading to superconductivity in the singlet channel. See Ref. [29].
- [44] Mayorov *et al.*, Nano Lett. **11**, 2396 (2011).

# Supplementary Materials of “Chiral Topological Superconductivity in CrO<sub>2</sub> bilayers”

Xu Dou, Kangjun Seo, and Bruno Uchoa\*

*Department of Physics and Astronomy, University of Oklahoma, Norman, OK 73069, USA\**

(Dated: February 3, 2019)

## I. TOPOLOGICAL PHASE TRANSITIONS

### A. Order of the transitions

In order to explicitly verify the existence of a quantum critical second order phase transition for  $|\mu| \gtrsim 0.18$  eV, when the system has a finite DOS at the Fermi level, we plot in Fig S1 the free energy for  $\mu = 0.1$  eV and  $\mu = 0.3$  eV. In the former, the topologically trivial superconducting state  $\mathcal{N} = 0$  coexists with the normal state at the critical coupling  $g_{1c} \approx 0.0919$  eV, where the order parameter is discontinuous. For  $\mu = 0.3$  eV, the transition to the normal state becomes continuous below  $\bar{g}_{1c} \approx 0.0561$  eV, when the system has a topological phase transition from the normal state to the  $\mathcal{N} = -3$  state. At  $g_{1c} \approx 0.078$  eV, the order parameter jumps, signaling the onset of a second topological phase transition to the  $\mathcal{N} = 1$  state.

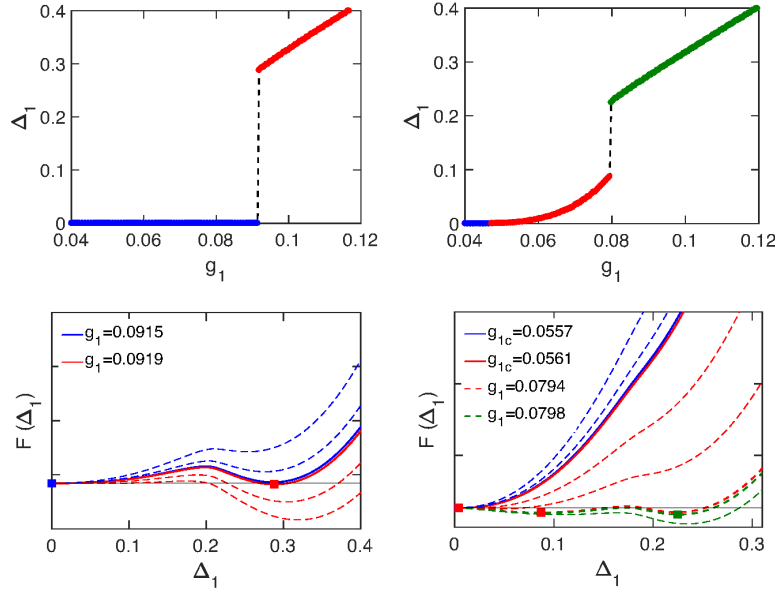


Figure 1: Top left: scaling of the intra-orbital coupling  $\Delta_1$  vs  $g_1$  for  $\mu = 0.1$  eV : first order phase transition from the normal to the superconductor state with  $\mathcal{N} = 0$ . Bottom left: Free energy for  $\mu = 0.1$  eV, showing the coexistence of the normal and superconducting states. Top right:  $\Delta_1$  vs  $g_1$  for  $\mu = 0.3$  eV. The system has a second order phase transition at  $\bar{g}_{1c} = 0.0561$  to a topological phase with  $\mathcal{N} = -3$  and a first order phase transition at  $g_{1c} = 0.078$  eV, where  $\Delta_1$  jumps. Bottom right: Free energy for  $\mu = 0.3$  eV, showing coexistence of the  $\mathcal{N} = -3$  and  $\mathcal{N} = 1$  states.

### B. Line of quantum critical points

Although the intra-orbital state is fully gapped, the Fermi surface at high doping is very anisotropic and produces an anisotropic superconducting gap in the energy spectrum around the Fermi surface. In Fig. S2 we plot the Fermi surface for  $\mu = 0.33$  eV and the corresponding energy gap along the Fermi surface, which has a significant variation. This anisotropic state requires a finite attractive coupling  $g_1$  to stabilize the formation of Cooper pairs, leading to a quantum critical phase transition even when the normal system has a large DOS at the Fermi level.

In Fig S3, we extract the quantum critical scaling of the order parameter  $\Delta_1$  with  $g_1$  in the vicinity of the critical point of the second order phase transition for  $\mu = 0.3$ , 0.312 (which coincides with the energy of a van Hove singularity)

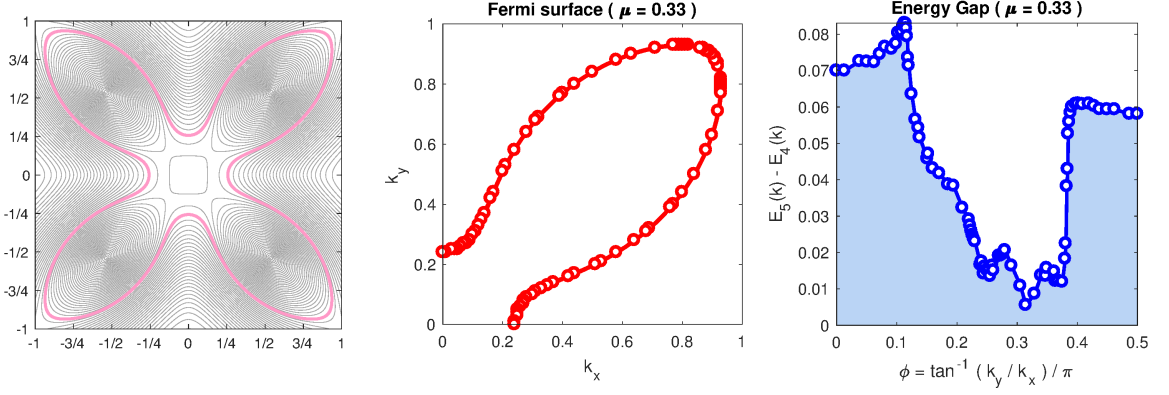


Figure 2: Left: Fermi surface for  $\mu = 0.33$  eV. Center: Path along the Fermi surface, where the energy gap in the superconducting state (intra-orbital gapped state) is calculated numerically in the weak coupling regime. Right: Anisotropic gap as a function of the angle  $\phi$  from 0 to 0.5 rad.

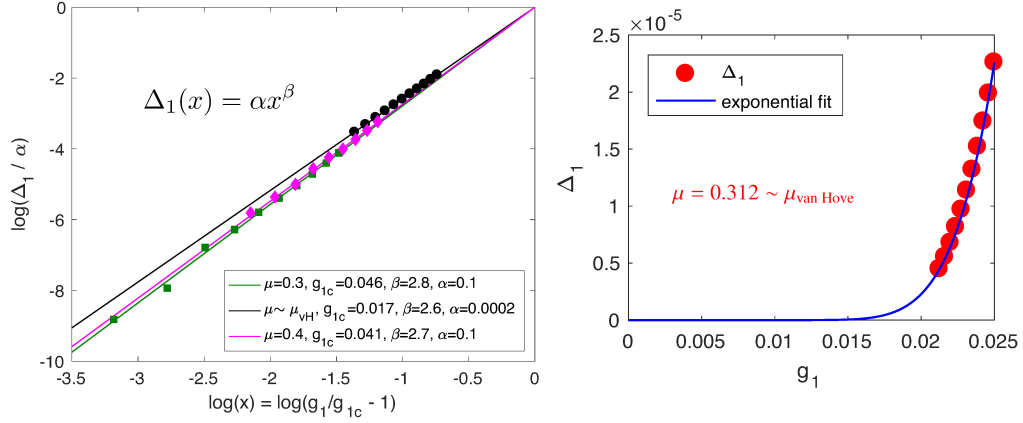


Figure 3: Left: Fermi surface for  $\mu = 0.33$  eV. Center: Path along the Fermi surface, where the energy gap in the superconducting state (intra-orbital gapped state) is calculated numerically in the weak coupling regime. Right: Anisotropic gap as a function of the angle  $\phi$  from 0 to 0.5 rad.

and 0.4 eV. The order parameter scaling has the form

$$\Delta_1(g_1) = \alpha \left( \frac{g_1}{\bar{g}_{1c}} - 1 \right)^\beta,$$

with  $\beta \approx 2.7 \pm 0.1$ ,  $\alpha = 0.1$  and critical couplings  $\bar{g}_{1c} = 0.046$  and  $0.041$  eV for  $\mu = 0.3$  and  $0.4$  eV respectively. However, at  $\mu = 0.312$  eV,  $\bar{g}_{1c}$  suddenly drops to  $\bar{g}_{1c} \approx 0.017$  eV and  $\alpha \approx 2 \times 10^{-4}$ . This abrupt drop in the numerical value of  $\bar{g}_{1c}$  suggests a crossover to exponential behavior due to the presence of a Van Hove singularity at the Fermi surface. In that scenario, the anisotropy of the gap around the Fermi surface as a whole becomes unimportant and the system likely becomes unstable towards superconductivity at any arbitrary attractive coupling, as in conventional Fermi liquids. At that filling,  $\Delta_1$  can fit well with an exponential curve  $\Delta_1 = \alpha / [\exp(\beta g_1) - 1]$ , with  $\alpha = 0.22$  and  $\beta = 4.36$ .

In the  $p_{x+y}$ -wave state, a power law scaling is also observed. In Fig. S4, we show the power law fitting of  $\Delta_1(g) = \alpha(g_1/\bar{g}_{1c} - 1)^\beta$ , where the exponent  $\beta(\mu)$  ranges from  $\beta \approx 0.79$  for  $\mu = 0.26$  eV to  $\beta \approx 2.9$  at  $\mu = 0.336$  eV. Near the van Hove, the critical coupling abruptly drops by one order of magnitude, suggesting exponential scaling.



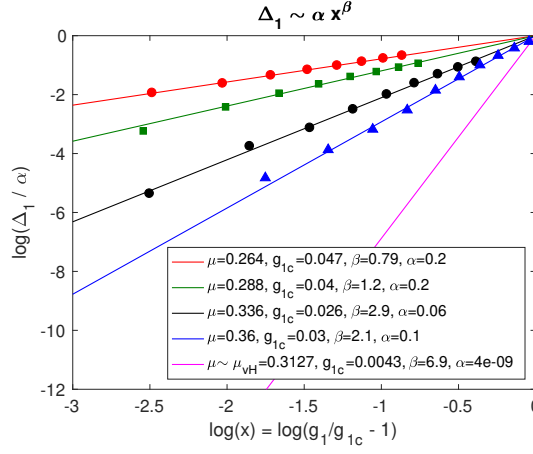


Figure 4: Power law fitting of the superconducting gap in the  $p_{x+y}$  state for different values of the chemical potential. At the van Hove singularity, the critical coupling drops abruptly, suggesting a crossover to exponential scaling.

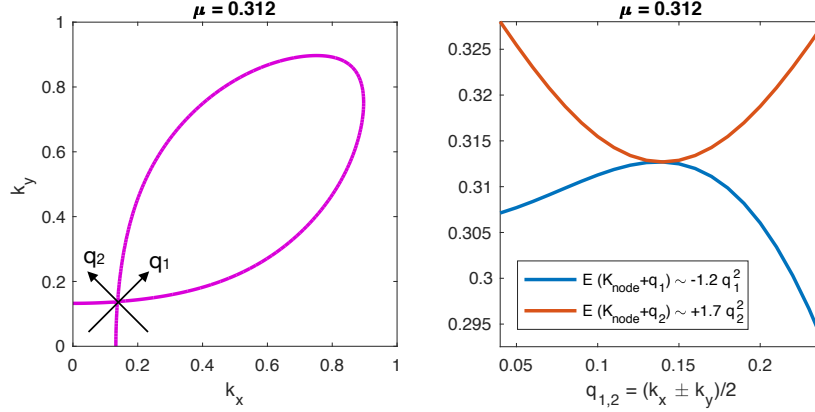


Figure 5: Left: Fermi surface at  $\mu = 0.312$  eV. The crossing indicates the position of the Van Hove singularity in the Brillouin zone for the tight-binding parameterization in the text. Right: Fitting of the bands around the van Hove singularity.

### C. $T_c$ estimate

Fig. S5 shows the Fermi surface at  $\mu = 0.312$  eV, where it crosses a saddle point indicated by the vectors  $q_1$  and  $q_2$ . On the right we fit the energy spectrum around that one saddle point. In general, the energy and position of van Hove singularities, as well as their dispersion, are not universal and are sensitive to the parametrization of the tight binding model. We assume the parametrization from ref. 1, which is based on ab initio results.

For a purely electronic mechanism, a crude estimate of the critical temperature can be calculated when the chemical potential is very close to the van Hove singularities of the band. For perfect nesting ( $\alpha = \beta$ ),

$$\chi_{ef} \approx \chi(\mathbf{Q}),$$

where

$$\chi(\mathbf{Q}) \sim \frac{1}{4\pi} \frac{1}{\alpha + \beta} \ln^2 \left( \frac{t}{|\mu|} \right)$$

has a double logarithmic divergence [2]. The effective interaction is

$$V_{ef} = \frac{U}{1 - U\chi_{ef}} \approx -\chi_{ef}^{-1}$$

when  $U\chi_{ef} \gg 1$ , with  $U$  the interaction between nearest sites. Since the DOS  $\rho(0) = \chi(0) = \frac{1}{2\pi^2\sqrt{\alpha\beta}} \ln(t/|\mu|)$ , the gap equation reads

$$1 \sim -\chi_{ef}^{-1} \int dE \rho(0) \frac{\tanh(E/2T_c)}{E} \sim -\chi_{ef}^{-1} \chi(0) \ln(\mu/T_c),$$

and hence

$$T_c \sim \mu e^{-\chi_{ef}/\chi(0)} \approx \mu \exp \left[ -\frac{\chi(\mathbf{Q})}{\chi(0)} \right] = \mu \exp \left[ -\frac{\pi}{4} \ln \left( \frac{t}{|\mu|} \right) \right] = |\mu| \left( \frac{|\mu|}{t} \right)^{\frac{\pi}{4}}.$$

This expression gives an upper bound for the critical temperature in the regime where  $\mu/t \ll 1$ .

#### D. Competition between $p$ and chiral $p + ip$ pairing at the saddle points

At the saddle points of the band, the order parameter can be broken into four patches related by the  $C_4$  symmetry of the bands combined with odd angular momentum of the Cooper pairs. In two opposite patches the order parameter has values  $\pm\Delta_a$ , and  $\pm\Delta_b$  for the other two. If the order parameters in different patches  $\Delta_a$  and  $\Delta_b$  are decoupled, the general Ginzburg-Landau free energy is

$$\mathcal{F}(\Delta_a, \Delta_b) = \alpha (|\Delta_a|^2 + |\Delta_b|^2) + \beta (|\Delta_a|^4 + |\Delta_b|^4) + \mathcal{O}(\Delta^6),$$

where  $\alpha = a_0(T - T_c) < 0$  in the ordered state and  $\beta > 0$ . Expressing  $\Delta_{a,b} = (\Delta_x^p \pm \Delta_y^p)/\sqrt{2}$  in a basis of  $p_x$  and  $p_y$  pairing states, then

$$\mathcal{F}(\Delta_x^p, \Delta_y^p) = \alpha (|\Delta_x^p|^2 + |\Delta_y^p|^2) + \beta (|\Delta_x^p|^2 + |\Delta_y^p|^2)^2 - \frac{\beta}{2} |(\Delta_x^p)^2 - (\Delta_y^p)^2|^2 + \mathcal{O}(\Delta^6).$$

At this order in the expansion, the free energy equally favors either  $\Delta_x^p \neq 0$  and  $\Delta_y^p = 0$  state (or the opposite combination), or else a coexistence phase between  $\Delta_x^p$  and  $\Delta_y^p$  with a  $\pm\pi/2$  phase difference, which has  $p_x + ip_y$  symmetry. At the mean field level, those two states are degenerate and have exactly the same free energy  $\mathcal{F} = -\frac{\alpha^2}{2\beta}$ . While the degeneracy can be lifted in higher order expansion, fluctuation effects are likely more important and should be taken into account.

---

\* Electronic address: [uchoa@ou.edu](mailto:uchoa@ou.edu)

- [1] T. Cai, X. Li, F. Wang, S. Ju, J. Feng, and C.-D. Gong, Nano Lett. 15, 6434 (2015).
- [2] P. C. Pattnaik, C. L. Kane, D. M. Newns, C. C. Tsuei, Phys. Rev. B 45, 5714 (1992).